Proceedings of the Institution of Mechanical Engineers, Part J: Journal of Engineering Tribology
http://pij.sagepub.com/

Comparison of fatigue model results for rough surface elastohydrodynamic lubrication

H Qiao, H P Evans and R W Snidle

Proceedings of the Institution of Mechanical Engineers, Part J: Journal of Engineering Tribology 2008 222: 381
DOI: 10.1243/13506501JET347

The online version of this article can be found at:
http://pij.sagepub.com/content/222/3/381

Published by:
SAGE
http://www.sagepublications.com

On behalf of:
Institution of Mechanical Engineers
Institution of Mechanical Engineers

Additional services and information for *Proceedings of the Institution of Mechanical Engineers, Part J: Journal of Engineering Tribology* can be found at:

Email Alerts: http://pij.sagepub.com/cgi/alerts

Subscriptions: http://pij.sagepub.com/subscriptions

Reprints: http://www.sagepub.com/journalsReprints.nav

Permissions: http://www.sagepub.com/journalsPermissions.nav

Citations: http://pij.sagepub.com/content/222/3/381.refs.html

>> Version of Record - Mar 1, 2008

What is This?

Downloaded from pij.sagepub.com at Cardiff University on April 4, 2012

Comparison of fatigue model results for rough surface elastohydrodynamic lubrication

H Qiao[1,2], **H P Evans**[1*], and **R W Snidle**[1]
[1]Cardiff School of Engineering, Cardiff University, Cardiff, UK
[2]Romax Technology, Nottingham Science and Technology Park, Nottingham, UK

The manuscript was received on 3 September 2007 and was accepted after revision for publication on 11 December 2007.

DOI: 10.1243/13506501JET347

Abstract: The paper compares the results of applying different fatigue failure models to surfaces that experience elastohydrodynamic lubrication (EHL) and have surface roughness features which are large compared with the equivalent smooth surface film thickness. The surface profiles used for the comparisons reported are taken from test gear surfaces used in an FZG gear test. The surface has a roughness of 0.31 μm Ra, with peak to valley dimensions of the order 1.5 μm. The tips of the asperities have been modified by running-in during the gear test. A transient EHL analysis was carried out using contacting components having this profile for a number of sliding speeds and nominal viscosity values. From these analyses, time-dependent pressure and shear stress distributions at the contacting surfaces were calculated. The resulting subsurface stress field was obtained relative to axes fixed in the moving surfaces using an elastic analysis so as to give the stress history at each point in a representative test section of the contacting component. A number of multi-axial fatigue criteria based on a critical plane approach were applied to the test section and the results compared. In addition, a varying amplitude multi-axial fatigue theory based on shear strain cycles was also applied to the section. The cycle counts were obtained using the rainflow counting method and the accumulated damage in a single pass through the contact area was calculated. In comparing the results obtained, the various fatigue models were found to identify the same asperity features as being those most prone to fatigue.

Keywords: rough surface elastohydrodynamic lubrication, surface fatigue, rolling contact fatigue

1 INTRODUCTION

The work reported in the paper is an attempt to apply a number of multi-axial fatigue models to the contact between gear tooth surfaces taking account of elastohydrodynamic lubrication (EHL) and surface roughness effects. The contacts considered replicate the situation in hardened and ground involute gears where the lubricant film thickness predicted between idealized smooth surfaces is considerably smaller than the height of surface asperity features. The ratio of the calculated smooth surface film thickness to the composite RMS roughness of the surfaces is referred to as the Λ ratio, and in gear contacts Λ ratio values as low as 0.1 are common. Under these conditions, the distribution of pressure developed between the surfaces is strikingly different from the smooth surface pressure profile, and local elastic pressures far in excess of the corresponding Hertzian values occur. Furthermore, the theoretical problem cannot be considered as quasi-static because of the transient effect of surface features as they move through the contact region. In spite of these difficulties, several numerical models of rough surface lubrication have been attempted [**1**–**5**]. A further complication which occurs under very low Λ ratio conditions is that of 'mixed lubrication' in which a degree of 'dry' contact occurs in an otherwise elastohydrodynamic, full-film situation. In order to obtain theoretical solutions under these conditions new numerical techniques have been developed [**6**, **7**] which have been used to predict transient 'dry' asperity interactions in both line and elliptical contacts. The present paper is concerned with the effect that

Corresponding author: Cardiff School of Engineering, Cardiff University, Queen's Buildings, The Parade, Newport Road, Cardiff CF24 3AA, UK. email: evanshp@cf.ac.uk

Downloaded from pij.sagepub.com at Cardiff University on April 4, 2012

the surface loading obtained from these solutions can be expected to have on the integrity of the contacting bodies due to high cycle fatigue at the surface asperity level. The measured surfaces used in the study are taken from the teeth of FZG test gears used in a study of micropitting damage.

Most of the work on prediction of surface fatigue in EHL contacts emanates from the rolling bearing industry. The classical approach to bearing life calculations is the work of Lundberg and Palmgren [**8**, **9**]. This method was developed and generalized by Ioannides and Harris [**10**] to a form that is now widely used. A simpler alternative was proposed by Zaretsky [**11**]. Researchers have considered the effects of surface dents and sinusoidal roughness features on these failure predictions [**12**, **13**]. Kim and Olver [**14**, **15**] have made analyses based on transient dry contact pressures between rough surfaces in rolling/sliding contact using the ideas of Ioannides and Harris [**10**] extended to account for 'microcycles' of stress during passage through the contact. Epstein *et al.* [**16**] have used representative transient pressure distributions obtained from EHL analyses incorporating different forms of surface roughness as the basis for fatigue calculations using the model of Zaretsky [**11**]. An alternative approach formulated in terms of crack propagation models has been proposed [**17**–**19**] based on smooth surface pressure distributions.

The loading imposed on transverse ground surfaces by their rolling/sliding contact is cyclic as asperity features move past each other, but the cycles are generally not equal to each other in amplitude, mean magnitude, or loading frequency. It is also likely that the loading is multi-axial, and models able to quantify fatigue effects in this complex situation are required. The simplest of these models, for example, those proposed by Crossland [**20**] and Sines [**21**], are based on invariants of the stress and deviatoric stress tensors. Others have sought to identify the direction of the critical plane where the fatigue damage is most prevalent, and a comparative study of a number of such models is given in reference [**22**]. The most complex approach is to reduce the loading history to a number of distinct cycles and to accumulate the damage caused by each such cycle according to the methods proposed by Palmgren [**23**] and Miner [**24**]. A number of methods for determining the appropriate cycles for a given loading pattern are presented in the literature and reviewed in reference [**25**]. For the current work, the rainflow counting method as implemented by Amzallag *et al.* [**26**] is used.

The purpose of the present study was to attempt to quantify fatigue in the near surface layer of gear tooth contacts as a means of explaining the micropitting phenomenon. This is a form of failure in gears associated with roughness effects characterized by small pits 5–10 μm deep, on the scale of the surface asperity features. In its most benign form, it is often seen as a type of mild wear, but it can develop with crack-branching leading to large scale pits that jeopardise the integrity of the gear and ultimately lead to catastrophic tooth breakage. In gear tests, micropitting is found to occur predominantly in the root area of the pinion and not in the tip of the meshing wheel, i.e. it generally occurs in the slower moving of the two surfaces (B. A. Shaw, Design Unit, University of Newcastle upon Tyne, 2003, personal communication). Surface asperities on the slower moving surface experience more load cycles in traversing the contact than do those on the faster moving counterface [**27**]. These findings suggest that a method responsive to stress cycling experienced by surface features as they traverse the EHL contact zone, and not solely to the extreme load experienced, is necessary to predict micropitting in gears.

2 THEORY

2.1 EHL and dry contact analysis

Evaluation of the different fatigue models considered is based on the results of a transient EHL line contact analysis for a pair of rough surfaces in rolling/sliding contact. The equations solved are the Reynolds equation for the lubricant and the plane strain elastic deflection equation for the (semi-infinite) solid bodies. A non-Newtonian lubricant behaviour is utilized which has been shown by Chang *et al.* [**3**] to be strongly influential in determining the solution to this transient problem for rough surfaces. The numerical technique is detailed in references [**6**], [**7**], and [**27**] and for a given nominal load involves solving the two equations simultaneously as a coupled pair. The elastic equation is formulated in differential form which allows the equations to be fully coupled within the solution scheme, and also allows a mixed lubrication analysis to be implemented at mesh points where the fluid film fails momentarily to separate the surfaces [**7**, **27**]. In the transient analysis, the faster moving surface is moved through a half mesh spacing in each timestep which has been shown [**6**] to ensure that changes with time are accurately resolved. The mesh spacing adopted is $\Delta x = a/200 \approx 1.7\,\mu$m which resolves typical asperity tip features for the roughness profiles adopted in the current study with around ten mesh points. The question of spatial resolution in this kind of analysis is addressed in reference [**27**]. The spatial derivatives are formulated with second-order accuracy using a finite-element scheme and the temporal derivative which is incorporated in a Crank Nicolson implicit scheme is second-order accurate in $\Delta t/2$ [**6**].

Downloaded from pij.sagepub.com at Cardiff University on April 4, 2012

2.2 Contacting body stress analysis

The stress components for an elastic body at a depth z within the contacting solids subject to pressure, $p(x, t)$, and shear stress, $q(x, t)$, acting on the surface is given by the integrals [**28**]

$$\sigma_x(x,z,t) = -\frac{2z}{\pi}\int_{x_1}^{x_2}\frac{p(s,t)(x-s)^2\mathrm{d}s}{[(x-s)^2+z^2]^2} - \frac{2}{\pi}\int_{x_1}^{x_2}\frac{q(s,t)(x-s)^3\mathrm{d}s}{[(x-s)^2+z^2]^2} \quad (1)$$

$$\sigma_z(x,z,t) = -\frac{2z^3}{\pi}\int_{x_1}^{x_2}\frac{p(s,t)\mathrm{d}s}{[(x-s)^2+z^2]^2} - \frac{2z^2}{\pi}\int_{x_1}^{x_2}\frac{q(s,t)(x-s)\mathrm{d}s}{[(x-s)^2+z^2]^2} \quad (2)$$

$$\tau_{xz}(x,z,t) = -\frac{2z^2}{\pi}\int_{x_1}^{x_2}\frac{p(s,t)(x-s)\mathrm{d}s}{[(x-s)^2+z^2]^2} - \frac{2z}{\pi}\int_{x_1}^{x_2}\frac{q(s,t)(x-s)^2\mathrm{d}s}{[(x-s)^2+z^2]^2} \quad (3)$$

On the surface, $z = 0$, the stress components can be determined by the boundary conditions

$$\sigma_z(x,0,t) = -p(x,t) \quad \tau_{xz}(x,0,t) = -q(x,t) \quad (4)$$

with σ_x obtained via Hooke's law and the Poisson effect [**28**] as

$$\sigma_x(x,0,t) = -p(x,t) - \frac{2}{\pi}\int_{x_1}^{x_2}\frac{q(x,t)}{x-s}\,\mathrm{d}s \quad (5)$$

The integrals in these equations are evaluated numerically using the discrete convolution fast Fourier transform (DC-FFT) technique described by Liu *et al.* [**29**]. This establishes the plane strain stress components in terms of coordinates (x, z, and t) with the origin of x and z fixed at the line contact point. The accuracy of this calculation with suitable zero padding has been shown to be equivalent to that of direct numerical integration of equations (1) to (3) [**30**]. Figure 1 illustrates the result of such a calculation at one particular timestep showing the surface loading and the corresponding stress distribution in the materials in terms of the von Mises equivalent stress.

The EHL problem is solved in axes fixed relative to the line of contact, and these are the coordinates x and z in the stress equations above. To establish the stress time history within the bodies as they move through the EHL contact area, the stress components need to be expressed in terms of axes fixed in the moving bodies. If (x', z') are the coordinates in terms of axes fixed

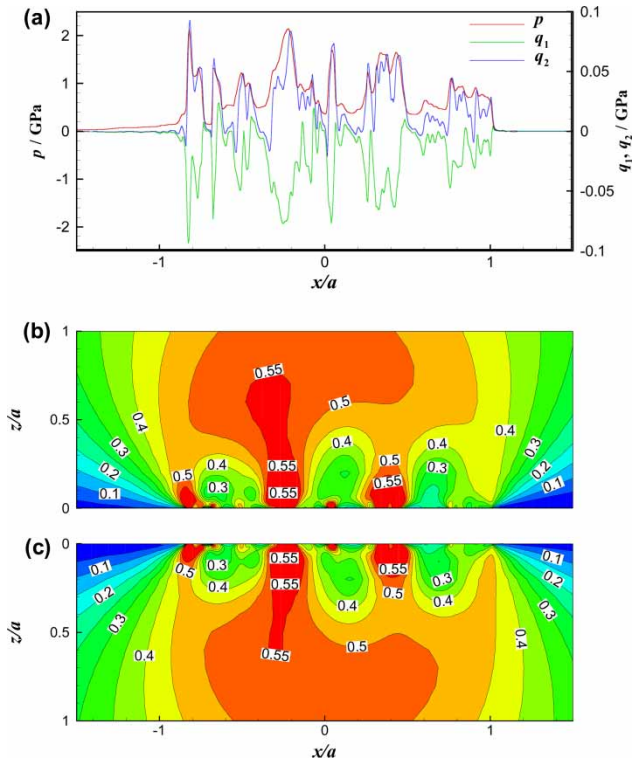

Fig. 1 Contours of σ_{vm}/GPa for the two rough surfaces which are subject to surface loading. (a) Pressure (p) and surface shear stress (q_1 for the upper surface and q_2 for the lower surface); (b) contours of σ_{vm} for the upper, faster moving solid; (c) contours of σ_{vm} for the lower, slower moving solid

in the material then

$$x' = x_{\mathrm{offset}} + x - ut \quad \text{and} \quad z' = z \quad (6)$$

where x_{offset} is the offset between the origins of the two coordinate systems at the start of the analysis and u is the surface velocity relative to the line of contact (either u_1 or u_2). The stress history is obtained by evaluating the stress components using equations (1) to (3) in the (x, z, t) axes and subsequently transforming to the (x', z', t) axes by interpolation in x. Alternatively the required positions where the stress components are needed can be specified directly in (x', z', t) coordinates but this complicates the DC-FFT approach to no advantage as the interpolation is straightforward.

This calculation leads to stress components being established at the specified (x', z') points for each of a series of timesteps in turn. It is then extremely beneficial to rearrange this data into the form of the time variation of the stress components at each (x', z') position in turn. This necessary sorting operation to establish the stress/time series at each material position is then only carried out once to generate a dataset to which any candidate fatigue model can be applied.

Downloaded from pij.sagepub.com at Cardiff University on April 4, 2012

For the comparative study of fatigue analyses reported here, rectangular blocks of material were considered whose dimensions were $2a$ parallel to the surface and a perpendicular to the surface as illustrated in Fig. 2. The blocks of material were discretized with a mesh of 201 uniform points parallel to the surface. Perpendicular to the surface, the mesh had points at $0.01a$ steps to a depth of $0.1a$, and at $0.1a$ steps thereafter. This spacing has no bearing on the calculation accuracy of the stress components which is determined by the EHL mesh spacing, but rather it specifies the points (x', z') at which the stress components are evaluated. The spacing adopted was found to be appropriate to resolve the variation in stress observed by comparison with evaluation over more finely subdivided calculation points. The most rapid spatial variation occurs in the 30 μm layer closest to the surface which is finely resolved. This can be clearly observed in the results of fatigue models discussed in the results section.

2.3 Critical plane fatigue analyses

A number of fatigue analyses of the critical plane type were carried out and compared, and the results of three such models of the fatigue process are presented in the current paper namely those due to Findley [**31**], Matake [**32**], and Dang Van *et al.* [**33**]. These criteria are not based on invariants of the stress tensor but postulate that fatigue will occur according to the value of a fatigue parameter, FP, which is a linear combination of a shear stress and a direct stress component and as such is a function of the orientation of the plane considered. The FP value is the value that this function takes in the (model defined) critical plane. The critical plane may be defined as the plane where FP is highest, or as the plane where one of the stress components

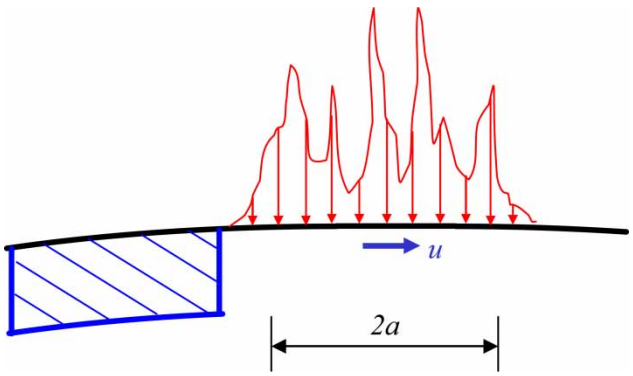

Fig. 2 Solid surface to which transient EHL pressure (red) and shear stress (not shown) distributions are applied showing block of material considered for fatigue analysis in the inlet region of the contact

is highest, according to the model adopted. The FP value is then compared with the corresponding value obtained in uniaxial fatigue tests for the same material. In the line contact case modelled in the current paper, the plane is inherently perpendicular to the Oxz plane and only the angle between the normal to the plane and the x-axis, θ_c, is to be determined.

From the stress history of each material point the mean shear stress, τ_m, and the shear stress amplitude, τ_a, can be defined as

$$\tau_m = \frac{\tau_{max} + \tau_{min}}{2} \qquad \tau_a = \frac{\tau_{max} - \tau_{min}}{2} \tag{7}$$

where τ_{max} and τ_{min} are the extreme values of shear stress obtained during the loading history in the orientation, θ, under consideration. Similarly $\sigma_{n,max}$ is the maximum value of the normal stress. The value of θ is varied from 0° to 180° in 1° steps in order to determine θ_c. The Findley criterion is based on the fatigue parameter defined as

$$\mathrm{FP}(\theta) = \frac{\tau_a(\theta) + \bar{\kappa}\sigma_{n,max}(\theta)}{\bar{\lambda}} \tag{8}$$

This is obtained as a function of θ, and the critical plane is given by the value of θ for which FP is greatest, θ_c. This maximal value of FP(θ) is then the value of FP established for the loading history applied to the material, that is

$$\mathrm{FP} = \frac{\tau_a(\theta_c) + \bar{\kappa}\sigma_{n,max}(\theta_c)}{\bar{\lambda}} \tag{9}$$

For critical plane models, the values of the constants $\bar{\kappa}$ and $\bar{\lambda}$ are determined from the fatigue limits obtained experimentally. Fully reversed bending and torsion tests [**34**] are used to establish, σ_{af}, which is the bending stress leading to fatigue in N_f repeated loading cycles in fully reversed bending and, τ_{af}, which is the shear stress leading to fatigue in N_f repeated loading cycles in fully reversed torsion. These are the bending and shear stress levels for which a particular number of repeated cycles lead to fatigue, e.g. $N_f = 10^7$ loading cycles. The critical plane model then postulates that fatigue failure will occur as a result of N_f repeated general loading cycles if the value of FP obtained for the general loading cycle is unity. For this hypothesis, correctly to identify the number of cycles to failure of the two fatigue experiments, constants $\bar{\kappa}$ and $\bar{\lambda}$ can be obtained from the experimental stress levels of σ_{af} and τ_{af} as

$$\bar{\kappa} = \frac{2 - (\sigma_{af}/\tau_{af})}{2\sqrt{(\sigma_{af}/\tau_{af}) - 1}} \qquad \bar{\lambda} = \frac{\sigma_{af}}{2\sqrt{(\sigma_{af}/\tau_{af}) - 1}} \tag{10}$$

In this work, the general loading cycle (referred to as the loading history) corresponds to one traverse of the test material through the EHL contact zone. In terms of

Downloaded from pij.sagepub.com at Cardiff University on April 4, 2012

gear tooth contacts it corresponds to one gear meshing cycle. Hence, when an FP value of unity is obtained, the critical plane model implies that fatigue failure is predicted to occur in N_f such meshing cycles. If a value greater than unity is obtained, the model implies that failure will occur in less than N_f such meshing cycles. Values of σ_{af} and τ_{af} are available as published experimental data for specific values of N_f representative of high cycle fatigue behaviour.

The Matake [**32**] fatigue criterion uses the same fatigue parameter (8) but the model differs from Findley's in that the critical plane, $\theta = \theta_c$, is taken as that on which $\tau_a(\theta)$ has its maximum, and the model constants are then

$$\bar{\kappa} = \frac{2\tau_{af}}{\sigma_{af}} - 1 \quad \bar{\lambda} = \tau_{af} \tag{11}$$

The Dang Van criterion [**33**] is more sophisticated than the critical plane criteria described above in that the time varying stress value is considered. If the mean shear stress τ_m is determined on a plane, then the current shear stress amplitude on the same plane is defined as [**35**]

$$\tau_a(t) = |\tau(t) - \tau_m| \tag{12}$$

where $\tau(t)$ is the shear stress at time t. The fatigue parameter for the Dang Van criterion is written as the combination of the current amplitude $\tau_a(t)$ and current hydrostatic stress $\sigma_h(t)$ on the plane

$$\mathrm{FP}(\theta) = \frac{\tau_a(t,\theta) + \bar{\kappa}\sigma_h(t)}{\bar{\lambda}} \tag{13}$$

and the critical plane is given by the value of $\theta = \theta_c$ for which FP is greatest when all values of t are considered, so that

$$\mathrm{FP} = \frac{\tau_a(t_c,\theta_c) + \bar{\kappa}\sigma_h(t_c)}{\bar{\lambda}} \tag{14}$$

where t_c is the time at which the maximal value occurs. Constants $\bar{\kappa}$ and $\bar{\lambda}$ are determined by fully reversed tests [**36**] as

$$\bar{\kappa} = 3\frac{\tau_{af}}{\sigma_{af}} - \frac{3}{2}; \quad \bar{\lambda} = \tau_{af} \tag{15}$$

2.4 Cumulative damage analysis

Under service conditions, the fatigue load can vary randomly, and variable amplitude fatigue behaviour models have been developed to achieve accurate lifetime predictions [**25**]. To deal with a random loading history, a cycle counting method is used to determine the effective loading cycles that it contains, and the corresponding stress levels for each effective loading cycle. The partial damage resulting from each effective loading cycle is then summed using a cumulative damage model. If multi-axial fatigue must be dealt with, the problem of random loading becomes extremely complicated. In the current work, the effective loading cycles identified, in general, correspond to heavy surface interactions as particular asperities on the rough surfaces move past each other in the rolling/sliding contact. For each part of the material there will be a number of such cycles during each pass of the material through the EHL contact area, with each such pass representing one gear meshing cycle.

The cycle counting scheme employed in the current paper is the widely used rainflow method which counts cycles by identifying closed hysteresis loops in the stress–strain response. The variant used in the current work is that proposed by Amzallag *et al.* [**26**].

The strain-life model adopted to establish the damage attributable to each effective loading cycle is that due to Fatemi and Socie [**37**] which is able to 'predict multi-axial fatigue life under both in-phase and out-of-phase loading conditions'. The strain-life equation is

$$\gamma_a\left(1 + K\frac{\sigma_{n,\max}}{\sigma_o'}\right) = \frac{\tau_f'}{G}(2N_f)^b + \gamma_f'(2N_f)^c \tag{16}$$

where γ_a is the amplitude of shear strain on the critical plane, and $\sigma_{n,\max}$ the maximum tensile stress normal to the plane, both evaluated for each of the individual loading cycles. K is a material constant, $K = 0.6$–1.0, G the shear modulus, and σ_o' the yield strength for the cyclic stress–strain curve. The shear fatigue strength, τ_f', and shear fatigue ductility coefficient, γ_f', are determined from fully reversed tests in pure shear. The fatigue strength exponent, b, and ductility exponent, c, are both negative and take the values -0.091 and -0.6, respectively, for this study.

To apply the Fatemi and Socie model, it is necessary to determine the subsurface stress and strain fields developed under the contact in the region of interest throughout the time taken for the material to pass through the EHL contact zone. As a first approximation, the stresses are evaluated assuming the stress field remains elastic (or experiences elastic shakedown under repeated contact if the contact pressure does not exceed the shakedown limit). The rainflow method is then used to identify the effective loading cycles at each point considered within the material. For each effective loading cycle, the values of γ_a and $\sigma_{n,\max}$ established are then used in equation (16) to determine the number of such loading cycles to failure, N_f. The total damage caused during a series of different effective loading cycles is then given by the Palmgren–Miner damage accumulation rule as

$$D = \sum_{\substack{\text{all effective}\\ \text{loading cycles}}} N_f^{-1} \tag{17}$$

Downloaded from pij.sagepub.com at Cardiff University on April 4, 2012

The value of D is determined for each point considered in the material for each possible orientation. The critical plane at each such point is that where the accumulated damage, D, is greatest, and fatigue failure is postulated to occur when D reaches a value of unity. When D is obtained in this way by summing over all of the effective loading cycles identified during one pass of the material through the EHL contact, i.e. for one gear meshing cycle, then the reciprocal of D is the number of meshing cycles to predicted fatigue failure.

2.5 Statistical behaviour

In order to extract statistical information from the fatigue analyses for the critical plane analyses, a form of the fatigue model proposed by Ioannides and Harris [**10**] was used to estimate the failure probability. The model can be written as

$$\ln \frac{1}{S} = \bar{A} N^e \int_V \frac{(\tau_e - \tau_u)^c}{z'^h} \, dV \tag{18}$$

where S is the probability of survival, N the fatigue life, τ_e the equivalent stress, τ_u the threshold fatigue limit stress below which no failure would occur, z' the stress weighted average depth, and V stressed volume. $\bar{A}$, e, c, and h are empirical constants to be determined from experimental data. The depth factor and the fatigue limit stress have been discussed by many researchers, e.g. references [**11**], [**15**], [**16**], and [**38**] and some of these authors prefer to ignore these parameters and the simpler form of equation (18) proposed by Zaretsky [**11**] is used in this study

$$\ln \frac{1}{S} = \bar{A} N^e \int_V \tau_e^c \, dV \tag{19}$$

The equivalent stress τ_e can be chosen based on multi-axial fatigue criteria in different ways. Ioannides *et al.* [**39**] listed some examples of criteria including maximum Hertzian pressure, orthogonal shear stress, maximum shear stress, maximum surface traction, von Mises stress and maximum shear amplitude regardless of plane and direction, and employed a Dang Van type modified shear stress in their fatigue analysis. This Dang Van type equivalent stress was also used by Kim and Olver [**14**, **15**]. Epstein *et al.* [**16**] used the octahedral stress in their fatigue analysis and stated that using different forms of equivalent stress had only a minor effect on the final results. In this study, the equivalent stress is calculated based on the Dang Van criterion of equation (14) as

$$\tau_e = \mathrm{FP} \times \bar{\lambda} = \max_t [\tau_a(t, \theta_c) + \bar{\kappa} \sigma_h(t)] \tag{20}$$

To assess the fatigue damage at a particular depth level, the probability of failure $F = 1 - S$ is determined. The exponents, e and c, take the values adopted by Ioannides and Harris [**10**]: $e = 10/9$ and $c = 31/3$. Following the strategy used by Kim and Olver [**14**], the parameter $\bar{A}$ is assumed to be related to the tensile strength of the material as follows

$$\bar{A} = \frac{1}{\sigma_u^c V_{\mathrm{ref}}} \tag{21}$$

where V_{ref} is the reference volume, which can be determined experimentally for a specific material. For comparative study of fatigue failures under different contact conditions, the actual value of V_{ref} is not important and is taken as the material volume considered in this study, i.e. $V_{\mathrm{ref}} = 2a \times a$. The element volume for a stressed point at a depth level is chosen as $\Delta V = \Delta x \times z_{\mathrm{ref}}$, where Δx is the mesh size in the x-direction and z_{ref} is a reference spacing in the z-direction for a depth level. A small value of $z_{\mathrm{ref}} = 10^{-4} a$ was chosen in this study by a trial and error approach. If z_{ref} is too large, the variation of the failure probability across the near surface layer, which has greatest stress gradients, may be overlooked. On the other hand, if z_{ref} is too small, then the calculated failure probability may be far smaller than unity. Therefore, the calculated F values obtained in this way are only stated for comparison. To predict actual fatigue failure probability in a practical application, experiments are required to determine these parameters in order to use the Ioannides–Harris model.

In considering the statistical distribution of the calculated fatigue damage, D, at a particular depth beneath the surface, its probability density function is naturally skewed towards low damage and the Weibull distribution is chosen as an appropriate stochastic model for this purpose. The damage distribution expressed in the three-parameter Weibull cumulative density function has the form [**40**]

$$F(D) = 1 - \exp\left[-\left(\frac{(D - \mu)}{\eta} \right)^{\beta} \right], \quad 0 \leqslant \mu \leqslant D, \ \ \eta, \beta > 0 \tag{22}$$

where η is the scale parameter, β the shape parameter, and μ the location parameter. To fit the distribution, the method of median rank regression is applied [**41**, **42**] to estimate β and η for given values of μ. The value of μ is then chosen as that which maximizes the corresponding correlation coefficient R^2.

3 RESULTS

The analyses reported were carried out for a rough surface profile obtained from previously reported [**43**] micropitting tests using an FZG gear testing machine. It has a roughness average of Ra = 0.31 μm and a trace

Downloaded from pij.sagepub.com at Cardiff University on April 4, 2012

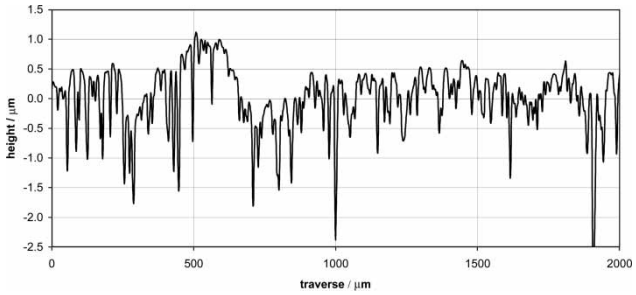

Fig. 3 Part of the surface profile used for the analyses

of the profile is shown in Fig. 3. This illustrates that the surface finish has a distribution of heights that has been skewed by the running-in process. The surface was run against itself in a transient EHL analysis using the methods reported in reference [**7**] so that comparisons could be made between the same portion of roughness profile in the fast and the slow surfaces. The analyses were undertaken in the context of high-speed aerospace gears and were run with the standard operating conditions specified in Table 1 using a model based on data for the synthetic lubricant Mobil Jet 2 at a nominal operating temperature of 100 °C. For cases where the calculated results indicate instances of mixed lubrication with direct asperity contact, a local coefficient of friction of 0.1 was adopted at the mesh points where the contact takes place. The material assumed for the two solids is SAE4340 (BS970:En24) and the parameters for the various fatigue models applied are also given in Table 1.

Figure 4 compares the contours of Fatigue Parameter obtained using the three critical plane models for EHL analysis using the parameters of Table 1. The results are for the trial section of the profile illustrated in Fig. 4 for the slower moving surface. Fatigue

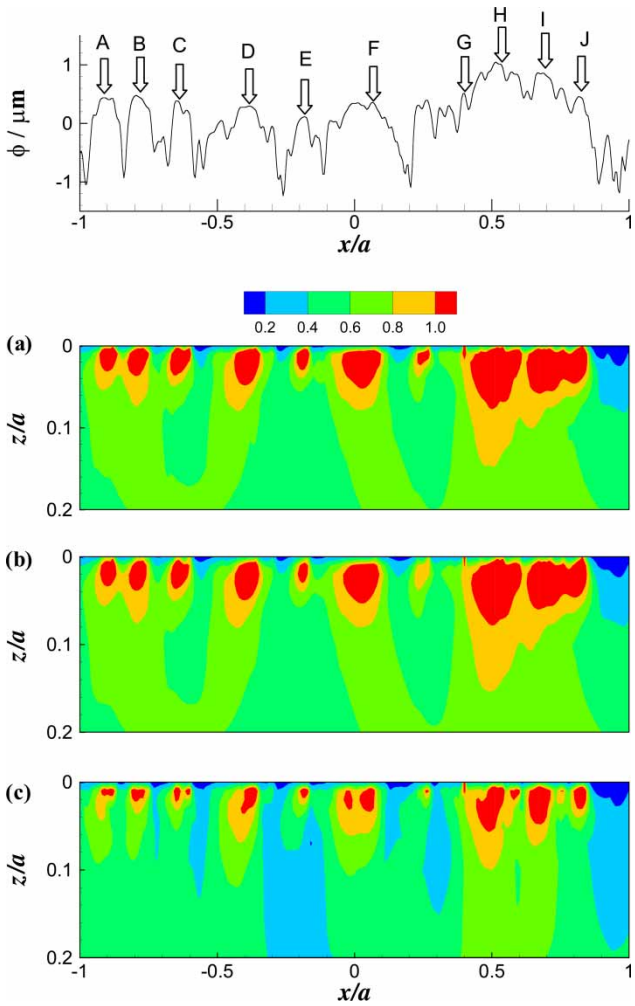

Fig. 4 Contours of fatigue parameter (FP) for fatigue at 10^7 cycles determined by using: (a) Findley, (b) Matake, and (c) Dang Van criteria. The upper graph shows the surface profile

Table 1 Parameters used for transient EHL line contact analysis

a	0.335 mm
E_1, E_2	200 GPa
p_0	1.0 GPa
R'	0.0191 m
w'	527 kN/m
ν_1, ν_2	0.3
$\bar{u}$	25 m/s
η_0	0.001 Pa s
ξ	0.5
σ_u	1.47 GPa
σ_{af}	695 MPa ($N = 10^7$)
τ_{af}	401 MPa ($N = 10^7$)
σ'_o	827 MPa
τ'_f	1.15 GPa
γ'_f	0.83
b	−0.091
c	−0.60
K	1.0

failure zones coloured red are those where FP $\geqslant 1$. It is clear that failure zones are concentrated near the surface of particular asperity features for the three criteria considered. The extent of the islands of high FP values calculated indicates that the material subject to fatigue damage is separated by areas that are subject to much lower loading levels from an FP value perspective. This suggests that micropitting could be expected in this kind of lubrication situation with micropits whose characteristic dimensions may be inferred from the typical sizes of the islands of high FP values. For the current example this dimension would be of the order 50 μm parallel to the surface, and the depth of the maximum FP values is about 10 μm. A summary of the application of these criteria to this analysis is presented in Table 2, which records ten asperities which have the highest FP values. The ten asperities are labelled with letters of A–J as identified in Fig. 4. It can

Downloaded from pij.sagepub.com at Cardiff University on April 4, 2012

Table 2 Ten identified asperities with highest FP values obtained using the three fatigue criteria

	Findley		Matake		Dang Van	
Rank	FP	Asperity	FP	Asperity	FP	Asperity
1	2.060	J	2.085	J	1.651	H
2	2.036	D	2.053	D	1.605	J
3	1.976	H	2.000	H	1.579	G
4	1.811	I	1.825	I	1.468	D
5	1.797	E	1.810	E	1.444	I
6	1.789	A	1.804	A	1.399	C
7	1.766	C	1.780	C	1.331	E
8	1.747	B	1.767	B	1.327	A
9	1.551	F	1.570	F	1.215	B
10	1.321	G	1.294	G	1.212	F

be seen that the Findley criterion and the Matake criterion give almost the same results. Using the Dang Van criterion, the calculated FP values are slightly lower for this case study and the sequence of asperities with decreasing FP values is reordered, but all three criteria agree on which asperities are those most likely to experience fatigue and, interestingly, which are not likely to experience fatigue. It is clear that loading is not wholly dependent on the shape of an individual asperity. There are aggressively shaped asperities within the profile that have low FP values associated with them. This is probably because they are sheltered from heavy interaction with counterface asperities by neighbouring, more prominent asperities. Indeed their aggressive shapes have probably survived to the loading stage at which the profile information was taken without being modified by plastic deformation because their prominent neighbours have protected them from heavy encounters.

Figure 5 presents curves giving the relative probability of failure F with depth for four contact conditions: (i) smooth–smooth, (ii) smooth–rough (smooth surface faster), (iii) rough–smooth (rough surface faster), and (iv) rough–rough. It can be seen that fatigue risks ranked according to severity are those of rough–rough, rough–smooth, smooth–rough, and smooth–smooth, and that when roughness is introduced to the contact the most vulnerable area is close to the surface, being within 20 μm of the surface in this example. For Case (iv), the probability of failure in this zone is three orders of magnitude greater than the maximum value for Case (i). Cases (ii) and (iii), which differ only in the speed of the rough surface, show different fatigue performance though it should be noted that the probability curve of Fig. 5 is for the slower moving surface. Thus it is for the rough surface in Case (ii) and the smooth surface in Case (iii). This phenomenon was observed by Kim and Olver [**15**] who concluded that sliding has no influence on Case (ii) but a significant influence on Case (iii). All four curves approach the same probability of failure in the zone where the roughness effect is no longer active.

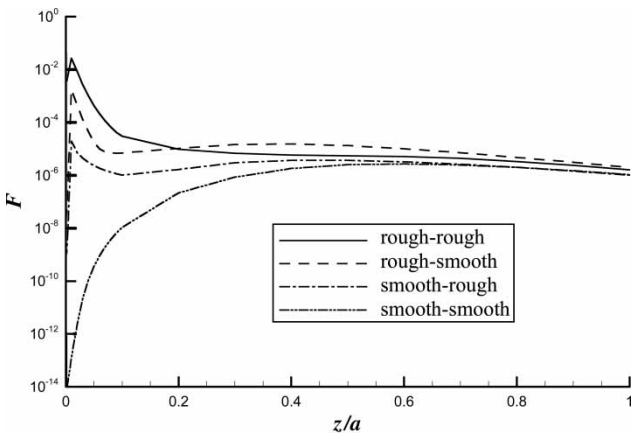

Fig. 5 Comparisons of fatigue failure probabilities versus depth for four contact conditions

Figure 6 shows the variation of fatigue parameter as the slide/roll ratio is increased. The results are all

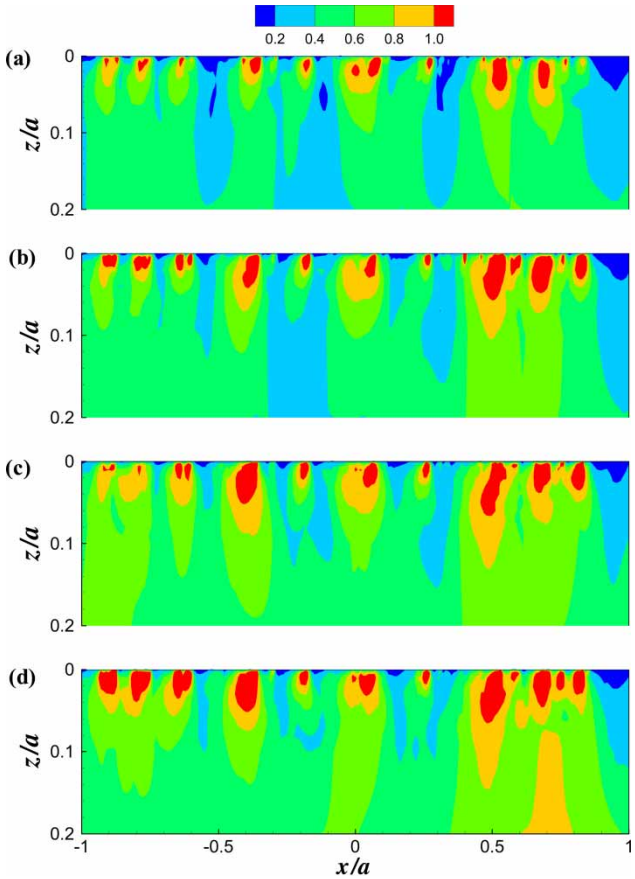

Fig. 6 Contours of fatigue parameter (FP) at 10^7 cycles obtained using the Dang Van criterion for the section of the slower moving surface illustrated in Fig. 4 with different slide roll ratio: (a) $\xi = 0.25$, (b) $\xi = 0.5$, (c) $\xi = 0.75$, and (d) $\xi = 1.0$

Downloaded from pij.sagepub.com at Cardiff University on April 4, 2012

obtained with the Dang Van criterion. When the sliding speed is higher, an individual asperity on the slower moving surface will interact with a longer portion of the counterface as it traverses the Hertzian area, and so it can be expected to have more loading cycles, and potentially experience higher FP values. This is confirmed by the increase in FP as the slide/roll ratio increases as seen in the figure. This increase is generally associated with the same asperity features, and there is no indication of 'protected' asperities, as described above, losing that protection as they experience more potential interactions with counterface asperities. It should be noted that in the analysis, the test block of material traverses from the inlet of the EHL calculation zone to the exit and when the sliding speed is changed it will interact with a different portion of the counterface.

Figure 7 shows Weibull cumulative distributions for results of the damage accumulation calculation for the standard case. The curves give the distributions at specific depths beneath the surface expressed as fractions of a. The damage is that calculated for a single pass through the contact zone and the curves give the probability that the damage level is greater than the abscissa value. Taking the curve for a depth of $z = 0.01a$ (=3.3 μm), for example, the distribution indicates that 30 per cent of the material at this depth has a damage value $D \geqslant 10^{-6}$, so that 30 per cent of the material would suffer fatigue in 10^6 or less passes through the contact zone. The figure indicates that the greatest accumulated damage is in the depth range 1.5–3.5 μm. The damage calculation presented statistically in Fig. 7 is also shown as one of the contour plots in Fig. 8, which compares calculated damage contours for the material within 70 μm of the surface for slide/roll ratios of between 0 and 1.5 with all other

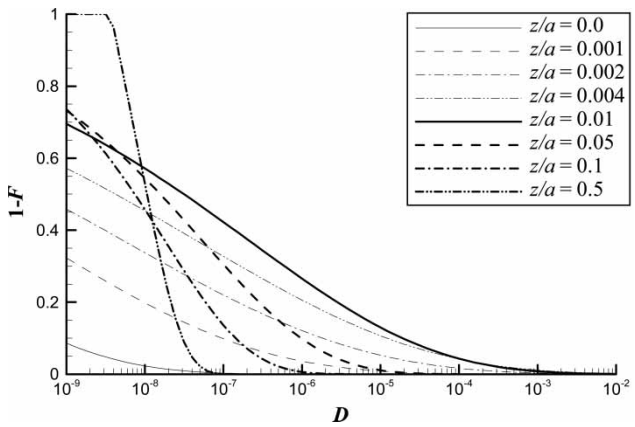

Fig. 7 Cumulative damage distributions for slower moving surface for the case with $\xi = 0.5$ and $\eta_0 = 0.001$ Pa s at a series of depths beneath the surface

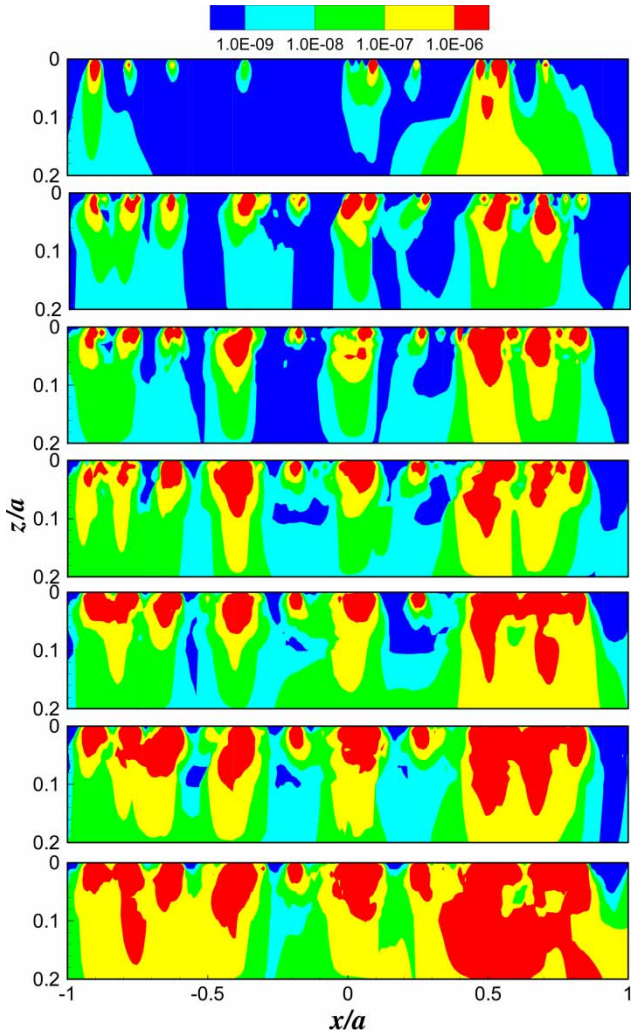

Fig. 8 Contours of subsurface damage calculated for the section of the slower moving surface illustrated in Fig. 4 during its transit of the contact area with $\eta_0 = 0.001$ Pa s and $\xi = 0$ (upper figure), 0.25, 0.5, 0.75, 1.0, 1.25, 1.5 (lower figure)

parameters unchanged. It may be compared directly with the critical plane analyses presented in Fig. 6. The highest contour level of $D = 10^{-6}$ represents a prediction of fatigue after 10^6 passes through the contact zone. For the upper contour plot corresponding to $\xi = 0$ (pure rolling), this level is reached at some five positions. As ξ increases to 0.75 further asperities reach this damage level. Further increases in sliding do not lead to any further centres of damage but rather to the damage level at each of the existing centres increasing. One further interesting feature of this comparison is seen at $x \cong 0.5$ for the $\xi = 0$ plot and at $x \cong 0.05$ for the $\xi = 0.5$ plot. At these positions it can be seen that a centre of damage is calculated very close to the surface and that a second centre of damage is obtained at the same asperity position but deeper

Downloaded from pij.sagepub.com at Cardiff University on April 4, 2012

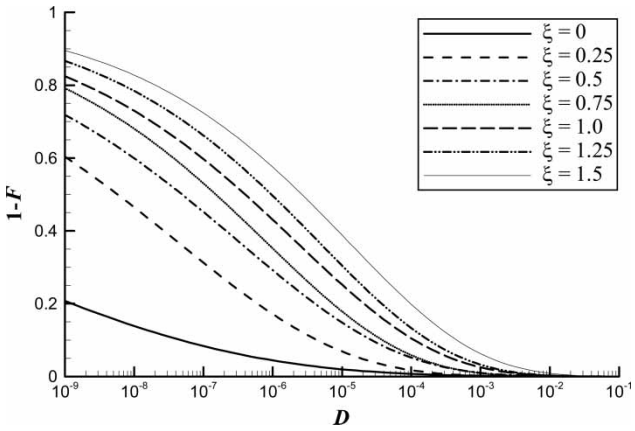

Fig. 9 Cumulative damage distributions at a depth of $z/a = 0.01$ beneath the surface for a series of ξ values

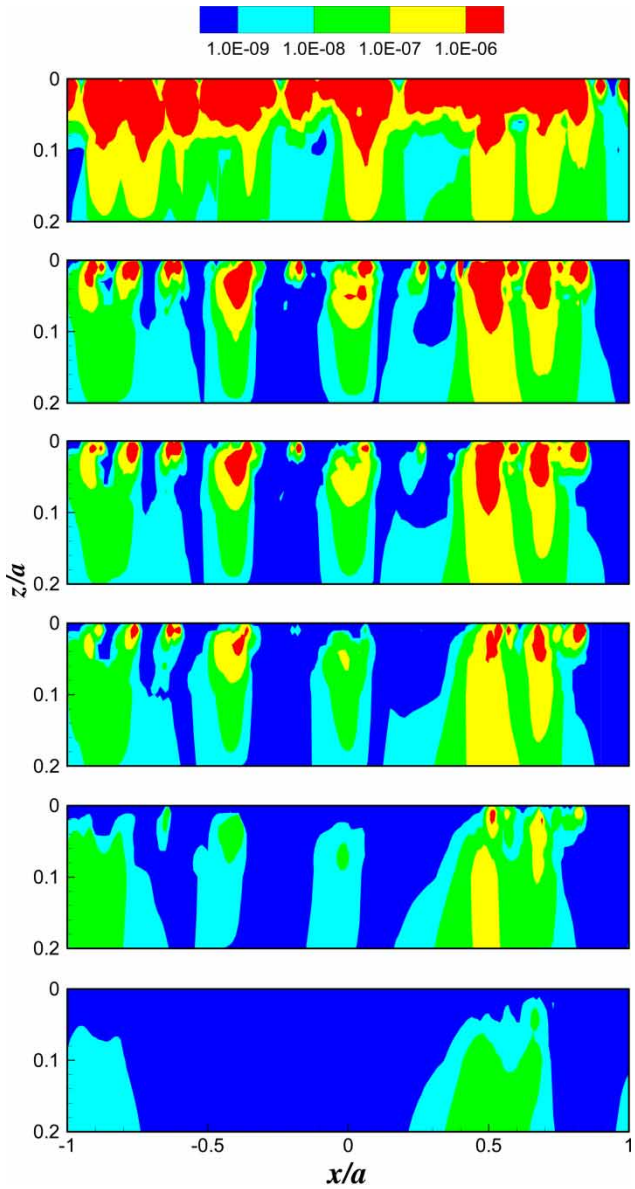

Fig. 10 Contours of subsurface damage calculated for the section of the slower moving surface illustrated in Fig. 4 during its transit of the contact area with $\xi = 0.5$ and $\eta_0 = 0$ (upper figure), 0.001, 0.002, 0.004, 0.008, 0.016 (lower figure) Pa s

beneath the surface. This feature is not seen in the corresponding calculations presented in Fig. 6. The systematic detrimental effect of increased sliding is identified clearly by the cumulative damage distributions for this set of calculations which are shown as a set for the $z = 0.01a$ depth in Fig. 9. In this figure, it is clear that each increase in slide/roll ratio moves the cumulative distribution to the right.

Fig. 10 illustrates the effect of progressively increasing the effectiveness of the lubricant film on the calculated damage contours. This was achieved by varying the viscosity of the lubricant between values of 0.001 and 0.016 Pa s. Also included in the series of contour plots is the result obtained for dry transient contact with an assumed friction coefficient of 0.1. This is the first of the contour plots and shows a damage level of 10^{-6} over almost all of the test material for a depth range of 0–20 μm. This damage intensity is effectively at a different scale in comparison with all of the lubricated results as the asperity contact pressures are much higher than those developed between the asperities in the lubricated contacts, and the boundary lubrication friction coefficient of 0.1 also leads to higher shear stress at the microcontacts. In introducing lubricant at the lowest viscosity of 0.001 Pa s, a dramatic reduction in the calculated fatigue damage is seen which is now centred at subsurface locations for the individual prominent asperities. Each subsequent doubling of viscosity causes further reductions in the calculated damage. These changes can be seen quantitatively in Fig. 11 which shows the cumulative damage distributions at the peak damage depth of $z = 0.01a$. Here, it is clear that introducing the lowest viscosity lubricant considered to the contact reduces the calculated damage by at least two orders of magnitude. An eight-fold increase in viscosity to 0.008 Pa s corresponds to a further reduction of approximately two orders of magnitude. These changes in the behaviour of the lubricated contacts are illustrated in terms of the contact Λ ratio in Fig. 12. The ordinate is the maximum value of D obtained for the analysis and this is plotted against the contact Λ ratio calculated from the smooth surface film thickness and the composite RMS roughness value, Rq. The dry contact result is not included on the figure but in terms of the ordinate of Fig. 12 has a maximum D value of 5265.

Downloaded from pij.sagepub.com at Cardiff University on April 4, 2012

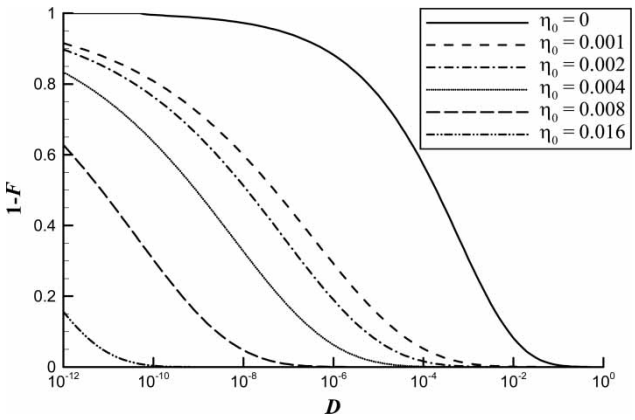

Fig. 11 Cumulative damage distributions at a depth of $z/a = 0.01$ beneath the surface for a series of η_0 values, $\eta_0 = 0$ indicates dry contact

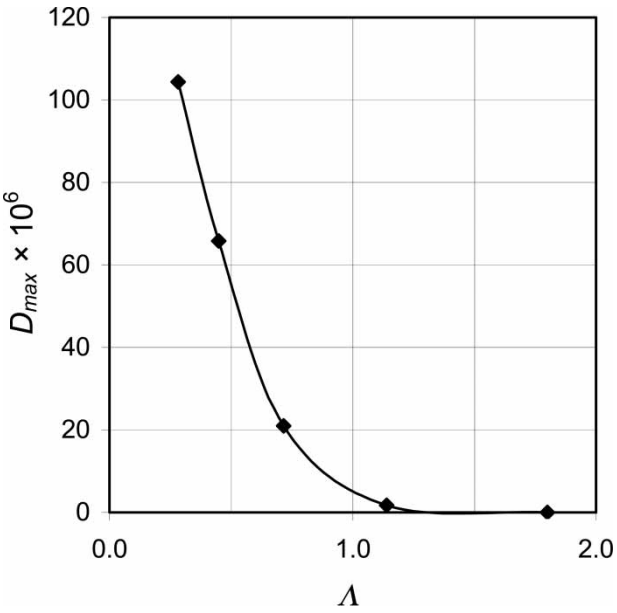

Fig. 12 Variation of $D_{\max}$ with Λ ratio for results obtained with different viscosity values

4 CONCLUSIONS

Transient microEHL analysis results have been used to generate time histories of stress at each material point. Both critical plane-based multi-axial fatigue criteria and cumulative damage theory have been applied in a comparative study. These give similar results for the particular gear tooth profile considered. Calculated damage is seen to be greatest close to the surface. Calculated damage is seen to increase with sliding speed and to decreases with increasing viscosity. Dry contact is significantly worse than lubricated contact from a calculated damage perspective

ACKNOWLEDGEMENTS

The work reported in this paper is associated with research funded by the EPSRC (GR/T05059) and by the European Commission (ADHER), which the authors gratefully acknowledge.

REFERENCES

1 **Venner, C. H.** and **Lubrecht, A. A.** Numerical simulation of a transverse ridge in a circular EHL contact under rolling/sliding. *Trans. ASME, J. Tribol.*, 1994, **116**, 751–761.

2 **Jiang, X., Hua, D. Y., Cheng, H. S., Ai, X.,** and **Lee, S. C.** Mixed elastohydrodynamic lubrication model with asperity contact. *Trans. ASME, J. Tribol.*, 1999, **121**, 481–491.

3 **Chang, L., Webster, M. N.,** and **Jackson, A.** On the pressure rippling and roughness deformation in elastohydrodynamic lubrication of rough surfaces. *Trans. ASME, J. Tribol.*, 1993, **115**, 439–444.

4 **Zhu, D.** and **Hu, Y.-Z.** A computer program package for the prediction of EHL and mixed lubrication characteristics, friction, subsurface stresses and flash temperatures based on measured 3-D surface roughness. *Tribol. Trans.*, 2001, **44**, 383–390.

5 **Wang, W.-Z., Liu, Y.-C., Wanh, H.,** and **Hu, Y.-Z.** A computer thermal model of mixed lubrication in point contacts. *Trans. ASME, J. Tribol.*, 2004, **126**, 162–170.

6 **Holmes, M. J. A., Hughes, T. G., Evans, H. P.,** and **Snidle, R. W.** Transient elastohydrodynamic point contact analysis using a new coupled differential deflection method. Part 1: theory and validation; Part 2: results. *Proc. Instn Mech. Engrs, Part J: J. Engineering Tribology*, 2003, **217**, 289–321.

7 **Holmes, M. J. A., Evans, H. P.,** and **Snidle, R. W.** Analysis of mixed lubrication effects in simulated gear tooth contacts. *Trans. ASME, J. Tribol.*, 2005, **127**, 61–69.

8 **Lundberg, G.** and **Palmgren, A.** Dynamic capacity of rolling bearings. *Acta Politech. Mech. Eng. Ser. R. Swedish Acad. Eng. Sci.*, 1947, **1**, 19–47.

9 **Lundberg, G.** and **Palmgren, A.** Dynamic capacity of roller bearings. *Acta Politech. Mech. Eng. Ser., R. Swedish Acad. Eng. Sci.*, 1952, **2**, 9–50.

10 **Ioannides, E.** and **Harris, T. A.** A new fatigue life model for rolling bearings. *Trans. ASME, J. Tribol.*, 1985, **107**, 367–378.

11 **Zaretsky, E. V.** Fatigue criterion to system design, life and reliability. *J. Propuls. Power*, 1987, **3**, 76–83.

12 **Coulon, S., Ville, F.,** and **Lubrecht, A. A.** Experimental investigations on rolling contact fatigue for dented surfaces using artificial defects. In Proceedings of the 31st Leeds–Lyon Symposium on *Tribology*, 2005, vol. 48, pp. 691–701 (Elsevier, Amsterdam).

13 **Chapkov, A. D., Colin, F.,** and **Lubrecht, A. A.** Influence of surface roughness on fatigue life. *Proc. IMechE, Part J: J. Engineering Tribology*, 2006, **220**, 287–294.

14 **Kim, T. H.** and **Olver, A. V.** Fatigue and brittle fracture analysis of surface engineered materials in rolling

Downloaded from pij.sagepub.com at Cardiff University on April 4, 2012

contact. In Proceedings of the 23rd Leeds–Lyon Symposium on *Elastohydrodynamics '96*, 1997, vol. 32, pp. 37–48 (Elsevier, Amsterdam).
15 **Kim, T. H.** and **Olver, A. V.** Stress history in rolling-sliding contact of rough surfaces. *Tribol. Int.*, 1998, **31**, 727–736.
16 **Epstein, D., Keer, L. M., Wang, Q. J., Cheng, H. S.,** and **Zhu, D.** Effect of surface topography on contact fatigue in mixed lubrication. *Tribol. Trans.*, 2003, **46**, 506–513.
17 **Keer, L. M.** and **Bryant, M. D.** A pitting model for rolling contact fatigue. *Trans. ASME, J. Lubr. Tribol.*, 1983, **105**, 198–205.
18 **Flašker, J., Fajdiga, G., Glodež, S.,** and **Hellen, T. K.** Numerical simulation of surface pitting due to contact loading. *Int. J. Fatigue*, 2001, **23**, 599–605.
19 **Kudish, I. I.** Lubricant-crack interaction, origin of pitting, and fatigue of drivers and followers. *Tribol. Trans.*, 2002, **45**, 583–594.
20 **Crossland, B.** Effect of large hydrostatic pressures on the torsional fatigue strength of an alloy steel. In Proceedings of the International Conference on Fatigue of Metals, London, The Institution of Mechanical Engineers, 1956, pp. 138–149.
21 **Sines, G.** Behaviour of metals under complex static and alternating stresses. In *Metal fatigue* (Eds G. Sines and J. L. Waisman), 1959, pp. 145–169 (McGraw Hill, New York).
22 **Papadopoulos, I. V., Davoli, P., Gorla, C., Filippini, M.,** and **Bernasconi, A.** A comparative study of multiaxial high-cycle fatigue criteria for metals. *Int. J. Fatigue*, 1997, **19**, 219–235.
23 **Palmgren, A.** DieLebensdauer von Kugellagern. *Z. Ver. Deutsch. Ing.*, 1924, **68**, 339–341.
24 **Miner, M. A.** Cumulative damage in fatigue. *J. Appl. Mech.*, 1945, **12**, 159–164.
25 **Downing, N. E.** *Mechanical behaviour of materials: engineering methods for deformation, fracture and fatigue*, 1993 (Prentice Hall, Englewood Cliffs, NJ, USA).
26 **Amzallag, C., Gerey, J. P., Robert, J. L.,** and **Bahuaud, J.** Standardization of the rainflow counting method for fatigue analysis. *Int. J. Fatigue*, 1994, **16**, 287–293.
27 **Holmes, M. J. A., Qiao, H., Evans, H. P.,** and **Snidle, R. W.** Transient effects in EHL point and line contacts having rough transverse surface finish. In Proceedings of the 30th Leeds–Lyon Symposium on *Tribology*, 2004, pp. 201–212 (Elsevier, Amsterdam).
28 **Johnson, K. L.** *Contact mechanics*, 1985 (Cambridge University Press, Cambridge, UK).
29 **Liu, S., Wang, Q.,** and **Liu, G.** A versatile method of discrete convolution and FFT (DC-FFT) for contact analysis. *Wear*, 2000, **243**, 101–111.
30 **Qiao, H.** *Prediction of contact fatigue for the rough surface elastohydrodynamic line contact problem under rolling and sliding conditions*. PhD Thesis, Cardiff University, 2005.
31 **Findley, W. N.** A theory for the effect of mean stress on fatigue of metals under combined torsion and axial load or bending. *Trans. ASME, J. Eng. Ind.*, 1959, **81**, 301–306.
32 **Matake, T.** Explanation of fatigue limit under combined stress. *Bull. JSME*, 1977, **20**, 257–264.
33 **Dang Van, K., Cailletaud, G., Flavenot, J. F., Le Douaron, A.,** and **Lieurade, H. P.** Criterion for high cycle fatigue failure under multiaxial loading. In *Biaxial and multiaxial fatigue, EGF 3* (Eds M. W. Brown and K. J. Miller), 1989, pp. 459–478 (Mechanical Engineering Publications, London).
34 **Carpinteri, A.** and **Spagnoli, A.** Multiaxial high-cycle fatigue criterion for hard metals. *Int. J. Fatigue*, 2001, **23**, 135–145.
35 **Ekberg, A.** Rolling contact fatigue of railway wheels – a parametric study. *Wear*, 1997, **211**, 280–288.
36 **Ciavarella, M.** and **Maitournam, H.** On the Ekberg, Kabo and Andersson calculation of the Dang Van high cycle fatigue limit for rolling contact fatigue. *Fatigue Fract. Eng. Mater. Struct.*, 2004, **27**, 523–528.
37 **Fatemi, A.** and **Socie, D. F.** A critical plane approach to multiaxial fatigue damage including out-of-phase loading. *Fatigue Fract. Eng. Mater. Struct.*, 1988, **11**, 149–165.
38 **Lubrecht, A. A., Jacobson, B. O.,** and **Ioannides, E.** Lundberg and Palmgren revisited. In *Rolling element bearings, towards the 21st Century*, October 1990, pp. 17–20 (Institution of Mechanical Engineering, London, UK).
39 **Ioannides, E., Jacobson, B.,** and **Tripp, J. H.** Prediction of rolling bearing life under practical operating conditions. In Proceedings of the 15th Leeds–Lyon Symposium on *Tribology*, 1989, pp. 181–187 (Elsevier, Amsterdam)
40 **Meeker, W. Q.** and **Escobar, L. A.** *Statistical methods for reliability data*, 1998 (John Wiley & Sons, New York).
41 **Abernethy, R. B.** *The new Weibull handbook*, 2nd edition, 1996 (Published by R. B. Abernethy) (ISBN 0-9653062-0-8).
42 **Ayyub, B. M.** and **McCuen, R. H.** *Numerical methods for engineers*, 1996 (Prentice Hall, New Jersey).
43 **Tao, J., Hughes, T. G., Evans, H. P., Snidle, R. W., Hopkinson, N. A., Talks, M.,** and **Starbuck, J. M.** Elastohydrodynamic lubrication analysis of gear tooth surfaces from micropitting tests. *Trans. ASME, J. Tribol.*, 2003, **125**, 267–274.

APPENDIX

Notation

a	Hertzian semi-contact dimension (m)
b	fatigue strength exponent
c	fatigue ductility exponent
D	accumulated damage fraction
E	elastic modulus (Pa)
F	cumulative density function of damage at given depth
G	shear modulus (Pa)
h	film thickness (m)
K	material constant in equation (16)
N, N_f	cycles to fatigue failure
p	pressure (Pa)
p_0	Hertzian contact pressure (Pa)
q	surface shear stress (Pa)
R'	radius of relative curvature of contact (m)
S	probability of survival

Downloaded from pij.sagepub.com at Cardiff University on April 4, 2012

t	time (s)
u_1, u_2	surface velocities in x-direction (m/s)
$\bar{U}$	entrainment velocity $= (u_1 + u_2)/2$ (m/s)
w'	load per unit length (N/m)
x	coordinate in rolling/sliding direction with origin at contact point (m)
x'	coordinate in rolling/sliding direction with origin fixed in the material (m)
z	coordinate normal to the surface with origin at contact point (m)
z'	coordinate normal to the surface with origin fixed in the material (m)
γ'_{f}	shear fatigue ductility coefficient
η_0	lubricant viscosity at ambient pressure (Pa s)
θ_{c}	orientation of critical plane
$\bar{\kappa}$	parameter in fatigue parameter definition (equation (8))
$\bar{\lambda}$	parameter in fatigue parameter definition (equation (8)) (Pa)
ν	Poisson ratio
ξ	slide roll ratio $= (u_1 - u_2)/(u_1 + u_2)$
σ_{af}	bending stress limit in fully reversed bending fatigue (Pa)
σ_{h}	hydrostatic stress (Pa)
σ_{n}	normal direct stress (Pa)
σ'_{o}	yield strength for the cyclic stress–strain curve (Pa)
σ_{u}	ultimate tensile strength (Pa)
σ_{vm}	von Mises equivalent stress (Pa)
σ_x, σ_z, τ_{xy}	material stress components (Pa)
τ_{a}	shear stress amplitude (Pa)
τ_{af}	shear stress limit in fully reversed torsion fatigue (Pa)
τ'_{f}	shear fatigue strength (Pa)

Downloaded from pij.sagepub.com at Cardiff University on April 4, 2012